8-2023

Computational and Experimental Study on Undoped and Er-Doped Lithium Tantalate Nanofluorescent Probes

Mkhitar A. Hobosyan

Andrea Pelayo Carvajal

Bhupendra B. Srivastava

Tamanna Zakia

Mohammed Jasim Uddin

See next page for additional authors

Authors

Mkhitar A. Hobosyan, Andrea Pelayo Carvajal, Bhupendra B. Srivastava, Tamanna Zakia, Mohammed Jasim Uddin, Karen S. Martirosyan, Eric Rodriguez, Kofi Nketia Ackaah-Gyasi, and Nicholas Dimakis

Computational and experimental study on undoped and Er-doped lithium tantalate nanofluorescent probes

Mkhitar A. Hobosyan[1], Andrea Pelayo Carvajal[1], Bhupendra B. Srivastava[2], Tamanna Zakia[2], Mohammed Jasim Uddin[2], Karen S. Martirosyan[1], Eric Rodriguez[3], Kofi Nketia Ackaah-Gyasi[4], and Nicholas Dimakis[1*]

[1]Department of Physics and Astronomy, UTRGV, Edinburg, TX, 78539

[2] Photonics and Energy Research Laboratory-PERL, Department of Chemistry, UTRGV, Edinburg, TX, 78539

[3]Department of Mechanical Engineering, University of Texas Rio Grande Valley, Edinburg, 78539, USA

[4]Department of Computer Science, University of Texas Rio Grande Valley, Edinburg, 78539, USA

Abstract

We present a combined computational and experimental work on lithium tantalate $LiTaO_3$ (LT) and its Er-doped counterparts. We use density functional theory under the generalized gradient approximation (GGA), to calculate the electronic and optical properties for both LT and $LT:Er^{+3}$, with Er occupying either Li or Ta sites, at 4.167 mol %. The GGA band structure calculations show that when Er substitutes Li, the Er-4f bands appear closer to the conduction band bottom, whereas when it substitutes Ta, they appear closer to the valance band top. This agrees with the higher peak in the imaginary part of the frequency dependent dielectric function at the band gap region for the former doped configuration relative to the latter. The electronic structure is also obtained using the HSE06 hybrid functional, for accurate location in energy for all 4f

---

[*] Author to whom correspondence should be made. E-mail: nicholas.dimakis@utrgv.edu

orbitals. We synthesized LT:Er^{+3} nanoparticles, validated through X-ray diffraction and Scanning Electron Microscopy. Differential scanning calorimetry and thermogravimetric analysis confirmed increases in the activation energy and lowering of the reaction temperature by Er^{+3} doping. Our photoluminescence examination showed strong emission in the visible and near-infrared regions and well correlated with the HSE06 electronic data, for doped configurations, verifying the Er f–f transitions.

Keywords: $LiTaO_3$; Er doping; Near-Infrared Detector; DFT; nanofluorescent probes; XRD; SEM; Differential scanning calorimetry

*E-mail: nicholas.Dimakis@utrgv.edu

1. Introduction

Lithium tantalate ($LiTaO_3$; LT) is a well-known as a highly stable crystalline material exhibiting exceptional properties such as photoelectric, piezoelectric, ferroelectric, and nonlinear optical material with high mechanical and chemical stability [1-3]. Doping LT with various rare-earth ions is used to achieve new optoelectronic properties [4-7]. Thin films of doped and pure LT layers have been extensively used for a wide range of applications [5, 8, 9]. The thin films on silicon made LT substrates are sensitive to violet light spectrum and can potentially serve as sensors [10]. LT single crystal films can be fabricated by ion slicing with promising properties as quick response pyroelectric devices [11]. LT thin films demonstrate nonlinear behavior, when subjected to short microwave pulses with pulse intensity altered over a wide range [12]. Lanthanum doped LT thin films show a lower energy gap, higher refractive index, and smaller particle size, when increasing the La_2O_5 dopant concentration [5]. Piezoluminescence was observed, when doping LT with Pr^{3+} ions [13]. Pr^{3+}/Gd^{3+} co-doping results in enhanced mechanoluminescence [14].

The preparation of nano-sized particles for both doped and pure LT remains challenging, although submicron particles have been synthesized using various techniques. The solution combustion method uses urea as fuel and inducer to reduce the duration and temperature of the reaction. Thus, LT doped with erbium III (Er^{+3}) oxide at various concentrations can be fabricated (LT:Er^{+3}) [15]. Molten salt method can also be used to synthesize Er^{+3} doped LT phosphors, by grinding the starting reagents with appropriate molar ratio and annealing the mixture to 850 °C [16]. The molten salt method can produce particles with sub-micrometer size, where LT begins to form at

400 °C and the reaction is completed, when the mixture is kept at 500 °C for 4 hours [17]. Smaller size particles can be fabricated along with the micrometer size grains, when mixing LT with LiCl-$CaCl_2$ and KCl-$CaCl_2$ at 700 °C and 750 °C [18]. The wet chemical method is more appropriate for fabrication of particles at nano-size range (nanosized powder), where the reaction temperature can be reduced to 450 °C [19]. Ultrafine sub-micrometer and nano-sized particles can also be fabricated with the sol-gel method, using ethylene glycol and polyethylene glycol as esterification and dispersant agents, respectively, with the calcination temperature ranging between 600-900 °C [20]. Calcination at high temperatures is one of the main reasons that large particles are synthesized. Thus, efforts are directed towards reducing the synthesis temperature [17, 21-23].

Density functional theory (DFT) [24, 25] calculations on LT have been reported [26-30]. Toksoy and Cabuk reported DFT calculated structural and electronic information, as well as elastic properties for ferroelectric and paraelectric LT phases [26]. The authors reported that the LT bandgap for both phases is indirect with values of 3.679 eV and 3.227 eV for the ferroelectric and paraelectric phases, respectively. Experimentally, the LT bandgap for the rhombohedral configuration was reported to be in the range of 3.93–5.06 eV [31-35]. Wang et al., reported LT bandgaps for both the rhombohedral and the cubic configurations using DFT and GW methods [27]. For the rhombohedral configuration, their DFT calculated bandgap was 3.93 eV, whereas their GW value was significantly higher at 5.58 eV. Riefer et al., reported DFT electronic and optical properties for LT, with calculated band gap of 3.71 eV [28].

The doped LT structure with Pr has been studied computationally by Tian et al. [36]. Shi et al. reported that doping LT with Er (LT:Er^{+3}) and Yb occurs at either the Li or the Ta sites [37]. The LT:Er^{+3} structural properties and its emission spectra have been probed experimentally [4, 37-39]. However, we are not aware of past reports on LT:Er^{+3} using computational approaches. Here, we report DFT electronic and optical properties calculations on LT and LT:Er^{+3} using the generalized gradient approximation (GGA) [40]. We examine the two cases for Er doping: In the first case, Er resides at the Li site and in the second case at the Ta site. The optical properties calculations include the frequency dependent dielectric function (real and imaginary parts), the refractive index, and the reflectivity. The LT and LT:Er^{+3} electronic information is also calculated using the hybrid functional HSE06 by Heyd, Scuseria, and Ernzerho [41] for accurate prediction of the energy location for the Er-4f bands. Our computational results are complemented by experiments. Specifically, we synthesize and study the LT and LT:Er^{+3} structures using X-ray diffraction (XRD) and scanning electron microscopy (SEM), whereas thermogravimetric analysis (TGA) is used to determine the lowest annealing temperature for the Er doped compounds. We use photoluminescence to investigate the effect of Er doping concentration on emission properties in both the visible and near infrared (IR) range.

2. Sample preparation and experimental methods

The chemicals used for this work are lithium hydroxide (LiOH; $\geq$ 98%, Sigma-Aldrich), tantalum (V) oxide (Ta_2O_5; 99%, Sigma Aldrich), ammonium hydroxide solution (ACS reagent, 28.0-30.0% NH_3 basis, Sigma Aldrich), hydrofluoric acid (ACS reagent, 48%, Sigma Aldrich) and erbium (III) oxide (Er_2O_3; <100 nm particle size, ≥99.9% trace metals basis, Sigma Aldrich).

Differential scanning calorimetry (DSC) (Q-600, TA Instruments) was used to study the LiOH-Ta_2O_5-Er_2O_3 reactions with heating rates in the range of 15-30 °C/min. The instrument has a mass resolution of 0.1 microgram, which provides the ability to work with very small amounts of reactants (~10 mg). The composition and the crystal structure of the powder was determined by XRD using a Bruker D-2 Phaser with Cu K_α anode, in 2θ range 20–80°, where the LT main peaks are distributed. The scans were taken with θ precision 0.02° and the sample was rotated with 15 rpm to statistically increase the number of particles contributing to XRD signal intensity.

The Ta_2O_5 was transformed to nano-size using the technique described in Ref. [19]. In this method, 0.28 g of Ta_2O_5 was dissolved in 5 ml of 48% HF in water heat bath at 75 °C for 8 hr. Afterwards, it was neutralized by ammonium hydroxide 30% solution, washed with deionized water, and centrifuged 3 times, followed by drying in oven at 100 °C for 12 hours. The thermogravimetric analysis showed 7.5 wt% remnant water in the Ta_2O_5, which was considered, when preparing the mixtures described below. The as prepared Ta_2O_5 was mixed with stoichiometric amount of LiOH and 0.5–10 mol. % of Er_2O_3 in acetone with zirconia balls using High Energy Ball Mill (HSF-3, MTI Co) machine for 5 minutes. The homogenized mixture was air dried, placed in the oven (GSL-1100X, MTI) that was programmed to reach 650 °C in 50 minutes and was kept at 650 °C for 4 hours. The final product was white ultrafine powder, which was analyzed using XRD, SEM, and photoluminescence measurements. Upconversion luminescence measurements were performed using an FLS 980 Edinburgh Instrument, which was equipped with an MDL–III–980-2W Class IV laser. For the DSC analysis, the initial powder mixtures of Ta_2O_5-LiOH and Ta_2O_5-LiOH-3mol% Er_2O_3 were used.

3. Computational modeling and calculating parameters

3.1. *Supercell modeling*

Fig. 1 shows the DFT-optimized LT 2 × 2 × 1 supercell in a triclinic form (space group *R3c*) with 24 Li, 24 Ta and 78 O atoms (126 atoms in total). Each Li and Ta atoms are coordinated with six oxygens in an octahedral symmetry. This supercell is used for both the LT and LT:Er^{+3} doped configurations. As stated above, we examine two doped configurations here both with 4.167% Er in the supercell. (Er substitutes Li or Ta). The LT:Er^{+3} doped configurations are still in a triclinic form, as the pure LT.

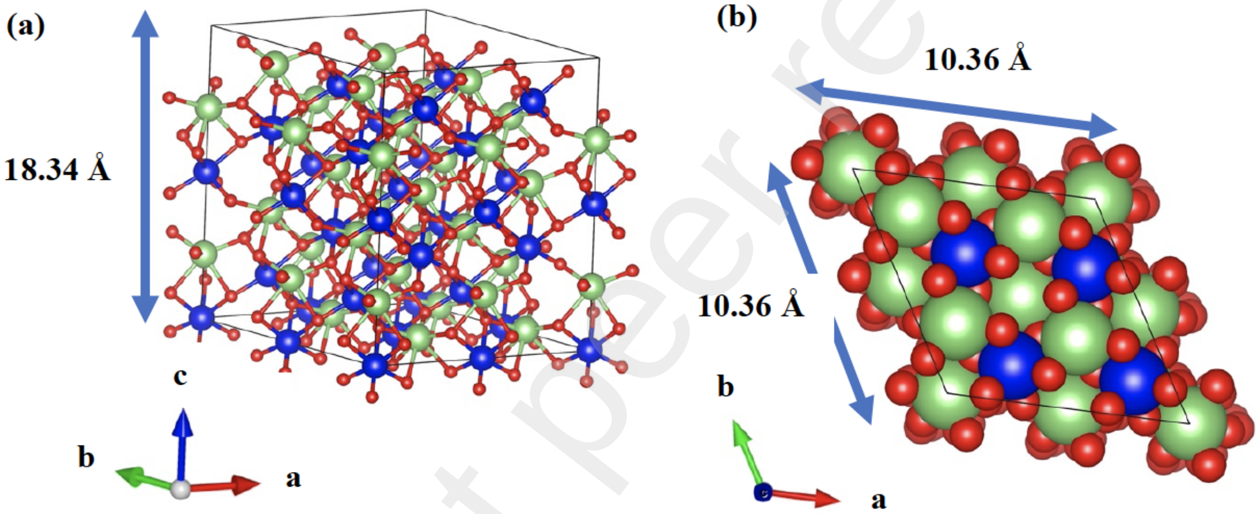

Fig. 1. (a) The side view of the $LiTaO_3$ (LT) optimized 2 × 2 × 1 supercell and (b) it's top view. Atoms are colored as follows: Li, green; Ta, blue; O, red. The thin lines denote the unit cell boundaries.

3.2. *Density functional theory parameters*

DFT electronic structure calculations, optimal geometries, and the dielectric functions were obtained for the LT host and its Er^{+3} doped counterparts using the periodic code Vienna *Ab initio* Simulation Package (VASP) [42-45]. The projector augmented-wave (PAW) pseudopotentials were used [46, 47]. The Kohn–Sham equations are solved using GGA under the Perdew–Burke–Ernzerhof (PBE) functional [40]. The band structure and the densities of states (DOS) were also obtained using the HSE06 hybrid functional, which improves the calculated band gaps values [48-52]. In all our calculations we included the D3 semiempirical correction by Grimme [53], which improves the DFT functionals descriptions for the long-range electron correlations (van der Waals interactions). The kinetic energy cutoff for all calculations is 600 eV, which ensures the integrity of our results. The energy convergence criteria were set at 10^{-9} eV and the geometry optimization criteria at 10^{-4} eV/Å per atom. The Brillouin-zone (BZ) was sampled using the Γ-centered 6 × 6 × 6 BZ grid.

We calculated Bader-type ion charges [54] using the Bader Charge Analysis code by Henkelman and co-workers [55-58], which partitions the charge density grid into Bader-type volumes. The code scales linearly with the number of grid points and can be used by large unit cells.

3.3. Optical properties

The frequency-dependent dielectric function is written as:

$$\varepsilon(\omega) = \varepsilon_R(\omega) + i\varepsilon_I(\omega) \qquad (1)$$

where $\varepsilon_R(\omega)$ and $\varepsilon_I(\omega)$ are its real and imaginary parts, respectively, and ω is the photon energy. The imaginary part $\varepsilon_I(\omega)$ is obtained computationally from the equation below [59, 60]:

$$\varepsilon_{I,j}(\omega) = \frac{\pi e^2}{2\varepsilon_0 m^2 (2\pi)^4 \hbar\omega^2} \sum_{c,v} \int_{BZ} dk \, |\langle U_{ck}|p_j|U_{vk}\rangle|^2 \delta(\omega_{ck}(k) - \omega_{vk}(k) - \omega)^2 \qquad (2)$$

where *e* and *m* are the electron charge and mass and $j = x, y, z$ and the summation is over the occupied and unoccupied states. The real part $\varepsilon_R(\omega)$ is calculated from the imaginary part $\varepsilon_I(\omega)$ via the Kramers-Kronig relation:

$$\varepsilon_R(\omega) = 1 + \frac{2}{\pi} \int_1^{\omega} \frac{\omega_1 \varepsilon_I(\omega_1) d\omega_1}{\omega_1^2 - \omega^2}. \qquad (3)$$

The refractive index $n(\omega)$, the extinction coefficient $k(\omega)$, and the reflectivity $R(\omega)$ are given in terms of $\varepsilon_R(\omega)$, $\varepsilon_I(\omega)$, $n(\omega)$, and $k(\omega)$ as follows:

$$n(\omega) = \left(\frac{[\varepsilon_R(\omega)^2 + \varepsilon_I(\omega)^2]^{\frac{1}{2}} + \varepsilon_R(\omega)}{2}\right)^{\frac{1}{2}}, \qquad (4)$$

$$k(\omega) = \left(\frac{[\varepsilon_R(\omega)^2 + \varepsilon_I(\omega)^2]^{\frac{1}{2}} - \varepsilon_R(\omega)}{2}\right)^{\frac{1}{2}}, \qquad (5)$$

$$R(\omega) = \frac{(n(\omega) - 1)^2 + k(\omega)^2}{(n(\omega) + 1)^2 + k(\omega)^2}. \qquad (6)$$

The optical properties are calculated using the independent particle approximation (IPA) [61]. The reported optical properties are averaged over the corresponding components parallel to x, y, and z axis. All the calculations were run on the Texas Advanced Computer Center (TACC) supercomputer facilities, using Stampede 2 and Lonestar 6 supercomputers.

4. Results and Discussion

4.1. LT nanoparticles synthesis

LT nanoparticles containing 0.5–10 mol. % Er were synthesized using the modified wet chemical synthesis method combined with annealing at 650 °C for 4 hours and utilizing modified Ta_2O_5 nanoparticles through the reaction,

$$2LiOH+Ta_2O_5 \rightarrow 2LiTaO_3+H_2O \quad (7)$$

XRD and SEM for tantalum oxide nanoparticles. The commercial Ta_2O_5 used in this work was initially a mixture of micrometer and nanometer sizes (Fig. S1a; Supplementary Materials). The Ta_2O_5 is highly crystalline, as evidenced by narrow XRD peaks (Fig. S1b). For this work, the Ta_2O_5 reagent was transformed to a more uniform nano-meter domain using the procedure described in the previous section. The as-prepared Ta_2O_5 particles have 100 nm average size (Fig. S1c) with wide XRD "hump" indicating amorphous structure (Fig. S1d). DSC/TGA shows that these particles contain about 7.5 wt. % water remnants. We have used the nano-sized Ta_2O_5 nanoparticles for the synthesis of $LiTaO_3$ and $LiTaO_3$-x(mol%)-Er nanoparticles for use in the photoluminescence experiments.

Differential scanning calorimetry (DSC) and thermogravimetric analysis (TGA) results. DSC combined with TGA analysis provide the weight change and heat flow as the sample is heated at selected heating rate. The integration of peaks for the heat flow curve is calibrated and provides absorbed (endotherm) or released (exotherm) energy per mass for the sample. The DSC/TGA analysis results for Ta_2O_5-LiOH and Ta_2O_5-LiOH-3 mol% Er_2O_3 are shown in Fig. 2. For the Ta_2O_5-LiOH system, the initial 9.7 wt. % weight loss with associated endothermic effect is due to the evaporation of remnant solvents and water trapped in Ta_2O_5 nanoparticles (Fig. 2a). An exothermic peak with 132.5 J/g released energy is detected starting at 548 °C with corresponding weight loss of 1.24 wt.%, which indicates the reaction between Ta_2O_5 and l LiOH, where the weight loss is due to the released water according to the reaction shown in (7). The reaction does not complete at this temperature, and the weight loss gradually continues as the temperature rises. There is another exothermic effect of 2974 J/g with peak at 888 °C which does not involve appreciable amount of weight loss and indicates crystallization [10].

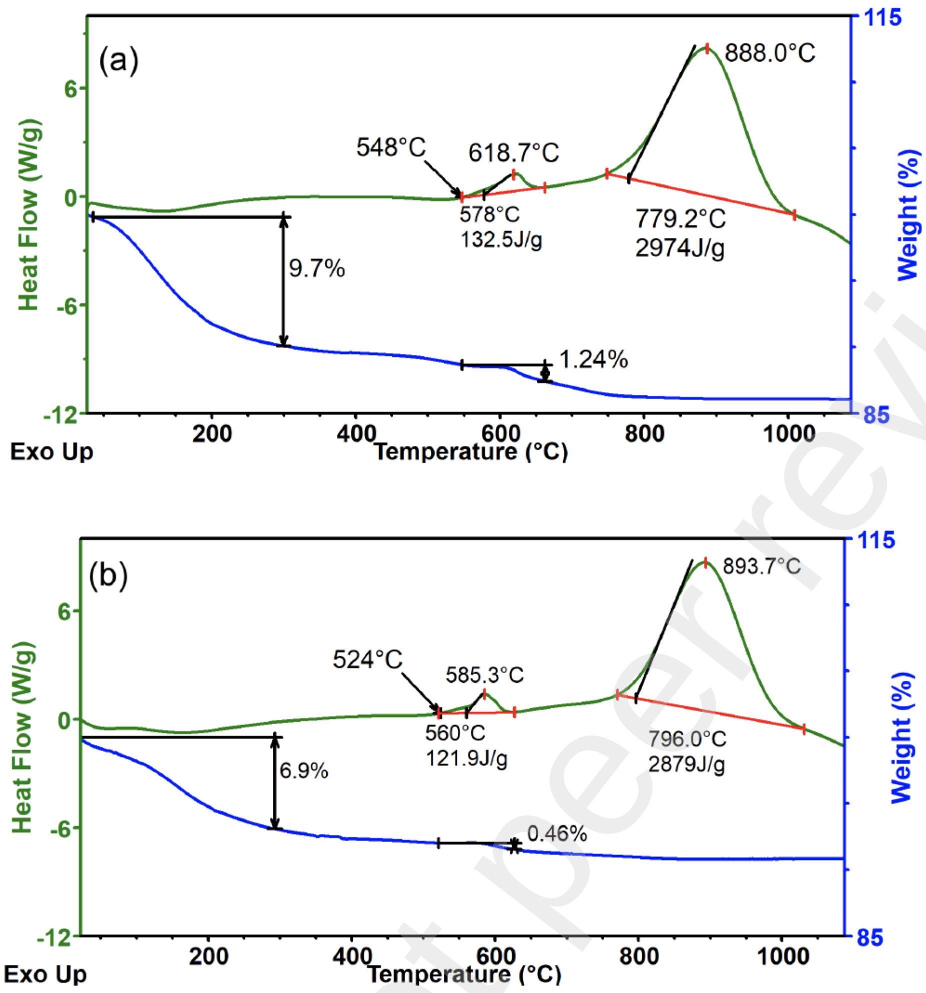

Fig. 2. DSC/TGA analysis results for (a) Ta_2O_5-LiOH and (b) Ta_2O_5-LiOH-3 mol% Er_2O_3 systems. The "Exo Up" label indicates that the exothermic effect is upward on heat flow curve.

The addition of 3 mol. % Er_2O_3 to the system reduces the reaction starting temperature to 524 °C (Fig. 2b). The exotherm effect is about 122 J/g, with 0.46 wt. % weight loss, indicating the removal of water according to the reaction (7). The initial 6.9 wt. % weight loss with associated endothermic effect is again due to evaporation of remnant solvents and water. The crystallization peak is at the same temperature range as for the system without Er_2O_3 with peak at 893.7 °C and similar energy release of 2879 J/g. The DSC analysis shows that the two systems are similar in nature with the reaction starting at slightly lower temperature for the system containing Er_2O_3. Both systems can be annealed at 650 °C to receive the desired product.

We estimated the activation energy for the Ta_2O_5-LiOH and Ta_2O_5-LiOH-3mol% Er_2O_3 reactions from DSC data using the isoconversional method suggested by Starink [62, 63] . In this method activation energy is determined by the following equation:

$$ln\left\{\frac{T^{1.8}}{\beta}\right\} = \left(1.007 - 1.2 \times 10^{-5} E_a\right)\frac{E_a}{RT} + const \quad (8)$$

where E_a is the apparent activation energy (in kJ/mol), β is the heating rate used in thermal analysis (in K/min), T is the peak temperature of the exothermic curve (in K), and R is the universal gas constant. E_a is estimated from the slope of the graph of $ln(T^{1.8}/\beta)$ vs. $1/T$. We estimated the activation energy in the Ta_2O_5-LiOH to be 138 kJ/mol (Fig. 3a), while the activation energy for the Ta_2O_5-LiOH-3mol% Er_2O_3 system was 263 kJ/mol (Fig. 3b). The addition of the Er_2O_3 in the mixture increases the activation energy while lowers the reaction initiation temperature as discussed for Fig. 2b. The increase of activation energy could be due to the incorporation of Er^{+3} (a larger ion) in the crystalline structure, while the initiation of the reaction at lower temperature could result from the presence of phase Er_2O_3 creating additional reaction spots in the system.

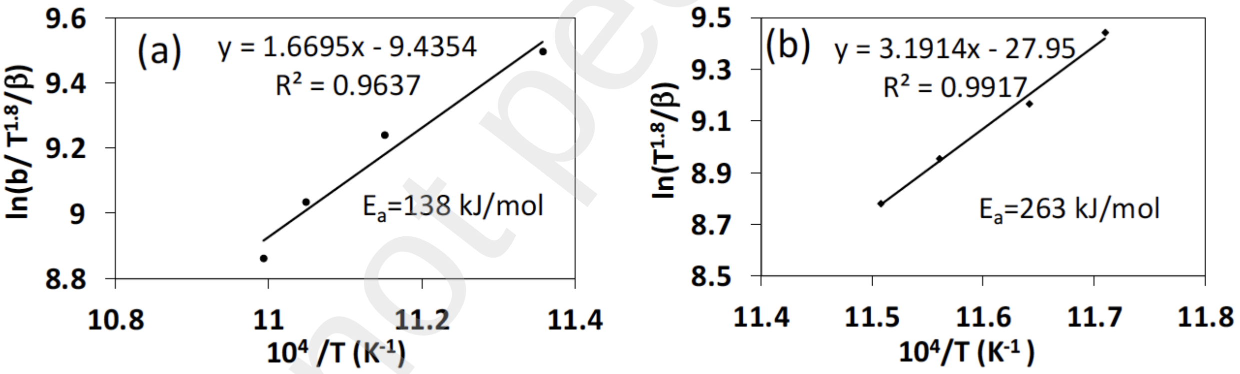

Fig. 3. Arrhenius plot for (a) - Ta_2O_5-LiOH and (b) Ta_2O_5-LiOH-3mol% Er_2O_3 system.

Based on the DSC/TGA results (Fig. 2a, b), for both Ta_2O_5-LiOH and Ta_2O_5-LiOH-3 mol% Er_2O_3 systems the annealing temperature was selected to be 650 °C kept for 4 h in furnace. Fig. 4 shows the XRD peaks for LT and LT:Er^{+3} at various Er doping concentrations and the SEM images. The SEM images show the morphology of the product received from Ta_2O_5-LiOH-3 mol% Er_2O_3 system. The as-prepared particles are in nanoscale range with average particle size 100 nm. Moreover, the XRD results of the product show stoichiometric $LiTaO_3$ structure, as shown in Fig 4 (left) with addition of 0.5 mol.% Er_2O_3. This could mean that the added Er ions do not change the crystallographic structure of LT when substituting either Li or Ta sites. When increasing the

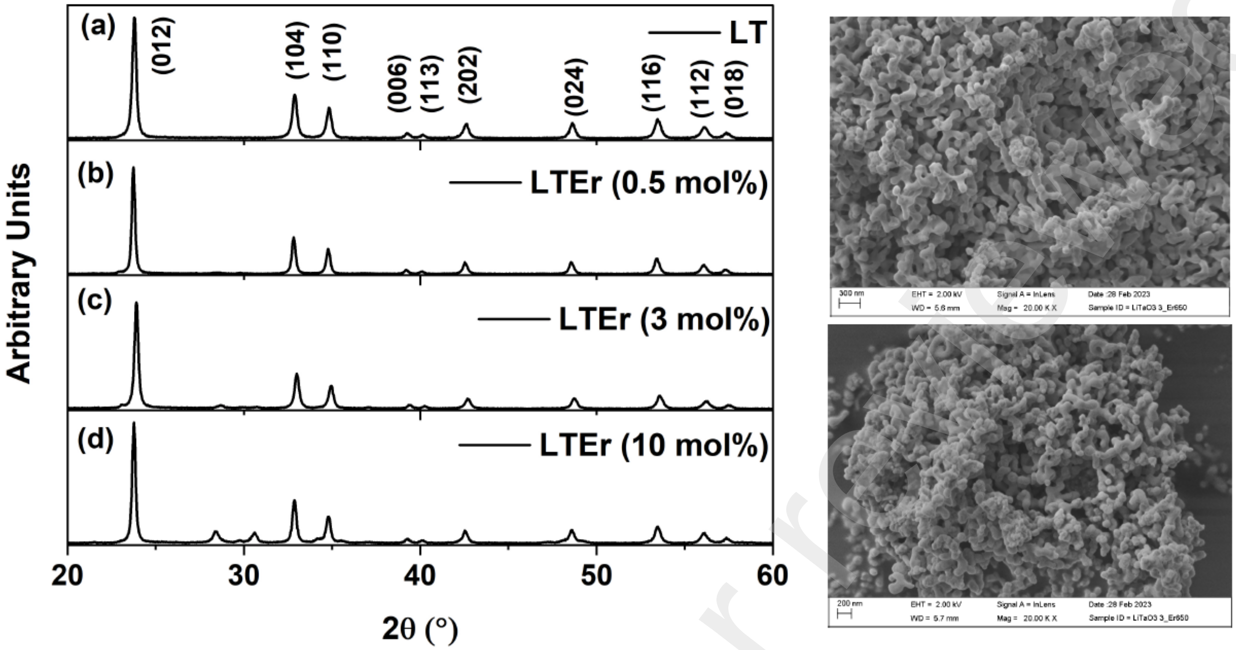

Fig. 4. Left. XRD analysis for (a) stoichiometric LT received from Ta_2O_5-LiOH and products received from (b) Ta_2O_5-LiOH-0.5 mol% Er_2O_3 (c) Ta_2O_5-LiOH-3 mol% Er_2O_3 and (d) Ta_2O_5-LiOH-10 mol% Er_2O_3 systems. Right. SEM images for the LT-3mol.% Er system.

amount of doping to 3 mol. % of Er_2O_3, we can notice a peak for Er_2O_3, indicating some excess of Er^{+3} oxide in the system. When the molar concentration of Er_2O_3 is increased to 10 mol. %, the XRD clearly shows the characteristic peaks of Er_2O_3 near 2θ = 28.5° and 30.7°, indicating that there is excess amount of Er_2O_3 in the system.

4.2. DFT calculated lattice parameters

Table 1 shows the calculated lattice constants for LT and LT:Er^{+3} of this work together with information on the metal-oxygen distances (metal is Li, Ta, and Er). For LT and LT:Er^{+3}, there are three longer and three shorter metal-O distances. Our calculated LT lattice parameters agree with past XRD results [19, 64]. Our *c* lattice parameter is larger relative to the experimental results by about 6 %. Doping with Er elongates the LT-Er *a* (and *b*) lattice parameters, whereas the *c* parameter appears smaller in the LT-Er, when Er substates Li and larger otherwise. Fig. S2 shows the simulated XRD spectra using the supercell of Fig. 1. Small changes in the lattice parameters due to doping are not evidenced from our experimental and simulated XRD data (i.e., no peak shifts are observed).

Table 1 shows that when Er substitutes Li or Ta in the doped configurations, the Er-O distances are larger than the corresponding Li-O and Ta-O distances.

Table 1. Lattice parameters and metal-oxygen interatomic distances for LT and LT:Er^{+3}. For the LT:Er^{+3}, the Li-O and Ta-O distances refer to atoms further away from the Er site in the supercell.

Structure	Lattice parameters		Interatomic distances		
	a (Å)	c (Å)	Li-O (Å)	Ta-O (Å)	Er-O (Å)
LT	10.29667	13.84594	2.021	1.929	
			2.311	2.068	
Exp.[19, 64]	10.304-10.308[1]	13.756-13.758			
LT:Er^{+3}(Er → Li)	10.36004	13.84132	2.028	1.937	2.207
			2.325	2.062	2.421
(Er → Ta)	10.31179	13.88917	2.014	1.934[2]	2.107
			2.313	2.064[2]	2.165

[1]Values adjusted to our supercell, [2]average distances.

4.3. Electronic structure information

LT band structure and DOS. Fig. 5 shows the calculated electronic band structure and the DOS for LT and LT:Er^{+3} under the GGA and the HSE06 (hybrid) functionals. Both calculations show similar profiles for the LT conduction bands bottom and its valance bands top. Moreover, they also show an indirect bandgap for LT, as expected [26]. The hybrid calculations show a significantly larger bandgap by about 1.41 eV relative to the GGA calculations. It is well-known that the HSE06 calculations improve the bandgap prediction relative to GGA [65]. Unfortunately, the hybrid functional calculations are time-consuming when plane wave-type basis sets are used. Therefore, for LT, the GGA calculated band structure and the DOS can mimic the corresponding HSE06 calculated properties by applying a rigid energy upshift to the conduction band. However, this is not the case for the doped LT:Er^{+3} configurations (vide infra).

For the LT, the DOS show that the O-p orbitals dominate in the valance band top, whereas the conduction band bottom is of Ta-pd orbitals. The same calculations show sp hybridization for Li-2s and -2p orbitals and Ta-6s and -6p orbitals. Therefore, these sp orbitals are partially populated, and appear above and below the Fermi energy. There is a significant overlap between the Ta-5d (and -6p) orbitals with the O-p orbitals, which is indicative of the strong covalent bonding between these two atoms. The overlap between the Li and O orbitals is small relative to the Ta-O orbital overlap. This suggests that Li-O bonds are weaker relative to Ta-O bonds, in agreement with the larger Li-O interatomic distances relative to the Ta-O ones.

LT:Er^{+3} band structure and DOS. For both LT:Er^{+3} configurations, the DOS and the band structure show the presence of the Er-4f bands, as expected. However, there are striking differences in the band structure between the two doping configurations examined here, as well as between the GGA and the hybrid calculations.

We first examine the doped configuration, where Er substitutes Li in the LT. The GGA calculations show that Er-4f bands are located at the Fermi energy and are mixed with the conduction band bottom. Here, the Er-4f bands occupy an energy region of about 0.2 eV (energy width of the band). At the GGA, these bands are located about 3.42 eV away from valance band top. However, the hybrid calculations show a splitting of these f-bands, which now appear above and below the Fermi energy. Specifically, the hybrid functional calculations show a collection of Er-4f bands below the Fermi energy between -0.8 eV and -1.95 eV, and an unoccupied band located at about 3.80 eV. The f-bands close to the Fermi energy are partially occupied and this statement applies to all doped configurations examined here. We must state that since DFT is a ground state method, the exact location in energy of the fully unoccupied 4f state is hard to be accurately determined. The band structure obtained from the hybrid calculations for the LT:Er^{+3} allows identification of the f–f transitions assignments, which is not possible using the GGA. Although these transitions are Laporte forbitten, these are possible due to mixing of the Er-4f states with its 4d states [66].

In the case that Er substitutes Ta, the GGA calculations show that the Er-4f bands are now mixed with the valance band top and are located 3.05 eV away from the conduction band bottom. In a similar fashion as above, the hybrid calculations show a split in the Er-4f bands, which are now located at 1.76 eV, -2.83 eV, and -4.38 eV relative to the Fermi energy. Here, the Er-4f bands, located below the Fermi energy are mixed with the O-p valance bands. This is in contrast with the configuration, where Er substitutes Li, where no mixing is observed between the Er-4f bands and the LT valance and conduction bands. Therefore, the selection of the Er doping site plays and important role in the LT:Er^{+3} electronic structure and consequently in its optical properties (vide infra).

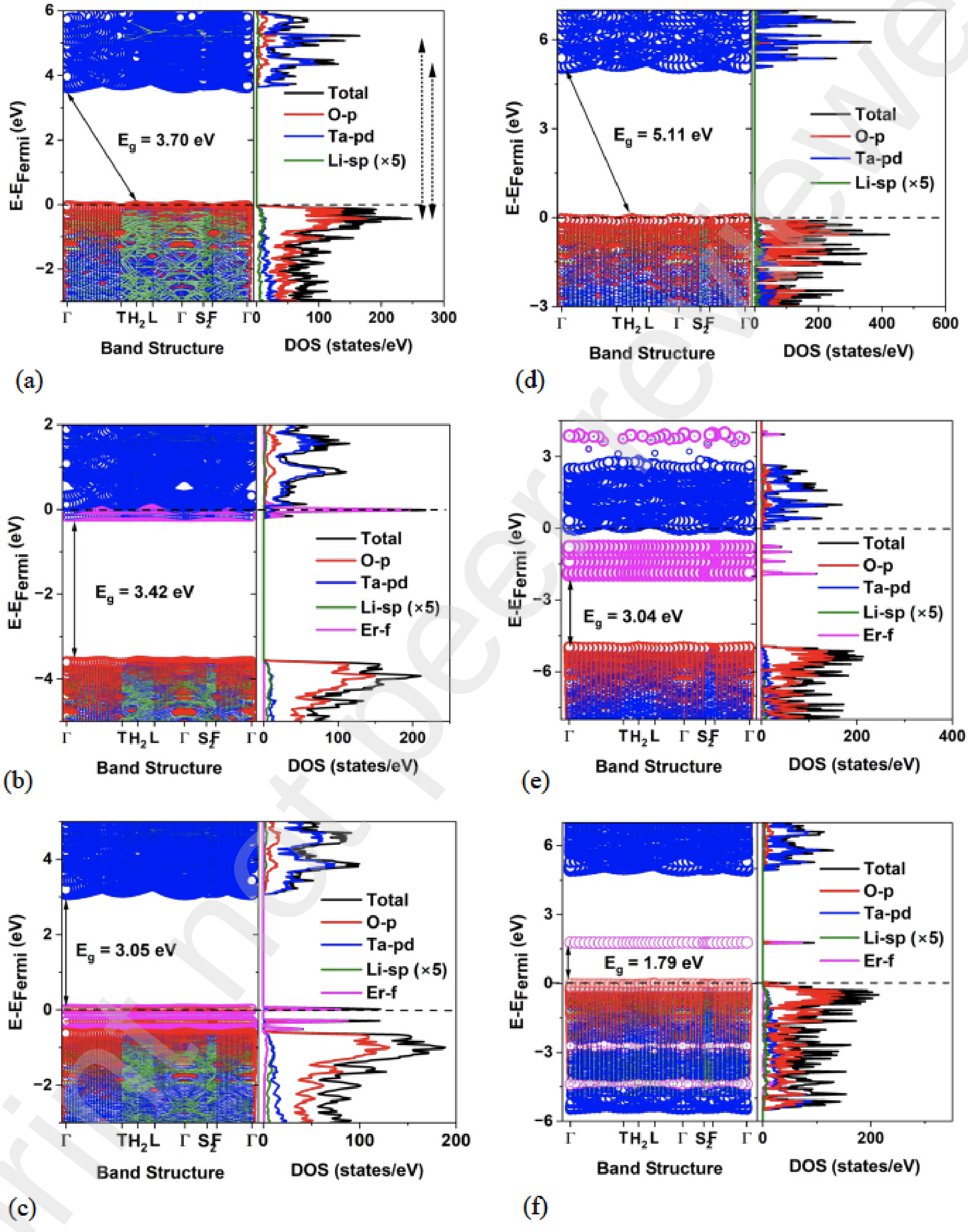

Fig. 5. Electronic band structure with orbital projections using the BZ path and the corresponding total and projected DOS per orbital using the PBE calculations for (a) LT, (b) LT:Er^{+3} (4.167% Er^{+3}) with Er to substitute Li, and (c) with Er to substitute Ta. (d), (e), and (f) show the corresponding HSE06 calculations for (a), (b), and (c), respectively. The dashed horizontal line is the Fermi energy (E_{Fermi}). The dotted vertical arrows denote electron transitions.

Charge analysis. The Bader charge analysis show that the host LT $LiTaO_3$ is mostly $Li^{0.87}Ta^{2.62}O^{-1.16}$. This is different from what is expected from the chemical formula (i.e., Li^{+1}, Ta^{+5}, and O^{-2}) and is indicative of the strong covalent Ta-O bonds. Similarly, for the Er doped configurations we get $Li^{0.87}Ta^{2.60}O^{-1.17}Er^{1.73}$ and $Li^{0.87}Ta^{2.62}O^{-1.14}Er^{2.07}$for the cases that Er substitutes Li and Ta, respectively. For LT:Er^{+3}, VASP hybrid calculations show the Er valance electron configuration as $s^{2.10}d^{0.48}f^{11.70}$ and $s^{2.14}d^{0.81}f^{11.01}$, when Er substitutes Li and Ta, respectively (electron configuration for isolated Er is $f^{12}s^2$). This shows that there are more Er f-type vacancies for the case that Er substitutes Ta. Similar trends are followed by the GGA calculations.

4.4. Calculated optical properties for LT and LT:Er^{+3}

Fig. 6 shows the real and the imaginary parts of the dielectric function ($\varepsilon_R(\omega)$ and $\varepsilon_I(\omega)$, respectively) for LT and LT:Er^{+3} with Er substituting Li and Ta atoms, as well as their refractive indices and the reflectivity. The optical properties have been calculated using the GGA approach, and therefore its information will be compared with the corresponding electronic structure obtained from the same level approximation. The peaks in the $\varepsilon_I(\omega)$ denote transitions from the valence bands to the conduction bands. The LT dielectric function's profile is similar to the one from the past reports from Cabuk [67] and Joshi et al. [68] for both the real the imaginary parts. Here, the $\varepsilon_I(\omega)$ is maximized at 4.80 eV and 5.5 eV, whereas another peak is evidenced at 9.15 eV. All these peaks correspond to transitions from the O-p states in the valence band to Ta-5d in the conduction band. The transitions that correspond to the $\varepsilon_I(\omega)$ maxima are shown in Fig. 5a. The $\varepsilon_I(\omega)$ onset value represents the bandgap. This value is 3.6 eV for LT and is close to the direct bandgap calculated from the electronic band structure (3.44 eV). The LT dielectric constant (i.e., $\varepsilon_R(0)$) is 4.9 and is increased upon doping with Er atoms (vide infra). The static refractive index $n(0)$ is about 2.24 and it increases to a maximum value of 3.34 at about 4 eV. High refractive index values have been indicative of the material to serve as heat preservatives and anti-reflection coatings. The high reflectivity value of about 40% at 5 eV is indicative that the material can serve as a mirror at UV ranges.

We now examine the changes in the LT optical properties due to doping with Er at Li or Ta sites. In both cases, the imaginary part of the dielectric function shows peak features at the bandgap region (Fig. 6a). However, there are minimal changes in the $\varepsilon_I(\omega)$ due to doping with Er for energies

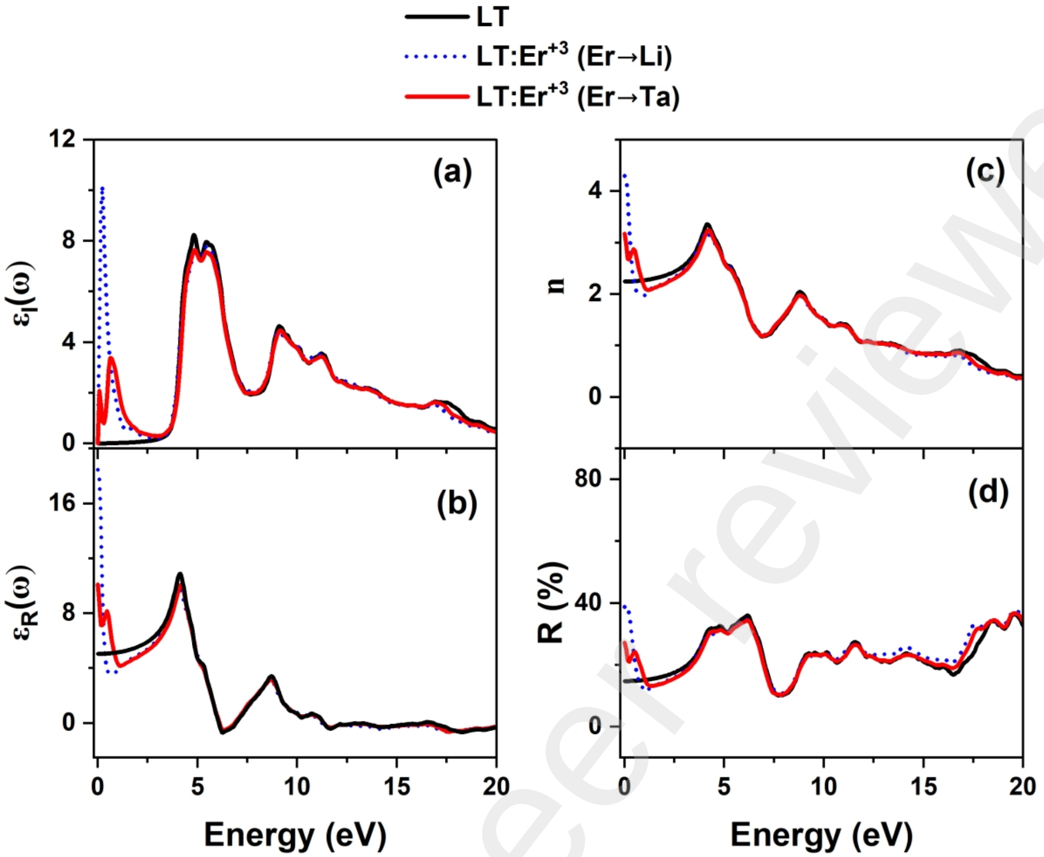

Fig. 6. a) The imaginary part of dielectric functions ε_I for LT and its Er doped counterparts for Er substituting Li (Er → Li) and Ta (Er → Ta) and b) the real part ε_R, c) the refractive index n, and d) the reflectivity R.

above the bandgap. This statement also applies to $\varepsilon_R(\omega)$, $n(\omega)$, and $R(\omega)$. The peaks in the bandgap correspond to transitions within the Er-4f band (intraband f–f transitions) and transitions that involve the Er-4f band orbitals and bands from the valance band top and the conduction band bottom, as stated previously. Specifically, for LT:Er^{+3} with Er substituting Li atoms, the GGA calculations show that the sharp $\varepsilon_I(\omega)$ peak, corresponds to both intraband f–f transitions and to the Er-4f –Ta-pd interband transitions. Similarly, for the doped configuration with Er substituting Ta atoms, the $\varepsilon_I(\omega)$ peaks in the bandgap include O-p – Er-4f interband transitions. The shaper peak for the case of Er substituting Li atoms is indicative of more vacancies, in agreement with the fact that in this case the Er-4f band is closer to the conduction band bottom.

The dielectric constant for the doped configurations is significantly larger than the one for the host, which is indicative that doping with Er makes LT:Er^{+3} a better dielectric material. The refractive index and the reflectivity of the LT:Er^{+3} are larger than the ones from LT for energies below about 0.9 eV, which correspond to IR and higher wavelengths. This means that the doped configurations can serve as improved heat preservatives and anti-reflection coatings mirrors relative to LT, as well as mirrors at both IR and UV regions.

4.5. Photoluminescence analysis and Er intraband transitions assignments

Fig. 7 shows the experimentally measured fluorescence emission spectra for LT with the free Er^{+3} transition assignments in the visible region and the near IR, as well as the DFT calculated Er-4f DOS using the HSE06 functional for LT:Er^{+3} with Er at the Li and Ta sites.

Photoluminescence analysis. The photoluminescence measurements show that the doped configuration with 3 mol% Er_2O_3 concentration provides much stronger emission in the visible wavelength with well separated peaks (Fig. 7a) compared to both 0.5 and 10 mol. % Er_2O_3 concentrations. The host LT ($LiTaO_3$) does not show emissions in the visible and near IR regions. This agrees with the calculated optical properties, which show no peaks in the bandgap region for LT. In addition, the Ta_2O_5-LiOH-0.5 mol% Er_2O_3 shows stronger emission in the near IR region, compared to the system containing 3 mol% Er_2O_3. The system containing 10 mol. % Er_2O_3 shows weak emission (Fig. 7b). Thus, for the visible region, the best doping concentration is 3 mol% Er_2O_3, while for the near infrared region the 0.5 mol% Er_2O_3 is more appropriate.

Er assignments. Crystal field theory shows that the isolated Er^{+3} has a ground state of $^4I_{15/2}$. This is since for Er^{+3} there are 11 4f electrons, which are distributed as follows: 2 electrons occupy the m_l states with values 0-3 and 1 electron occupy the states m_l states -3, -2, and -1. The f states are f_{z^3} ($m_l = 0$), f_{xz^2} and f_{yz^2} ($m_l = \pm 1$), f_{xyz} and $f_{z(x^2-y^2)}$ ($m_l = \pm 2$), and $f_{x(x^2-3y^2)}$ and $f_{y(3x^2-y^2)}$ ($m_l = \pm 3$). However, the HSE06 calculations show a different ground state (Fig. 7c,d) than the one corresponds to the free Er^{+3}, since in the doped configurations the Er oxidations are +1.72 and +2.07. For both doping configurations the Er-4f states with $m_l = 0, \pm 3$ are occupied, whereas all other 4f states are partially occupied. The broadening of the Er-4f for the LT:Er^{+3} with Er occupying the Ta sites is due to mixing of these orbitals with the valance bands (i.e., O-p) of the host. Here, we have identified the Er f–f transitions for both configurations using the calculated Er-4f DOS spectra, which correspond to emissions from the photoluminescence.

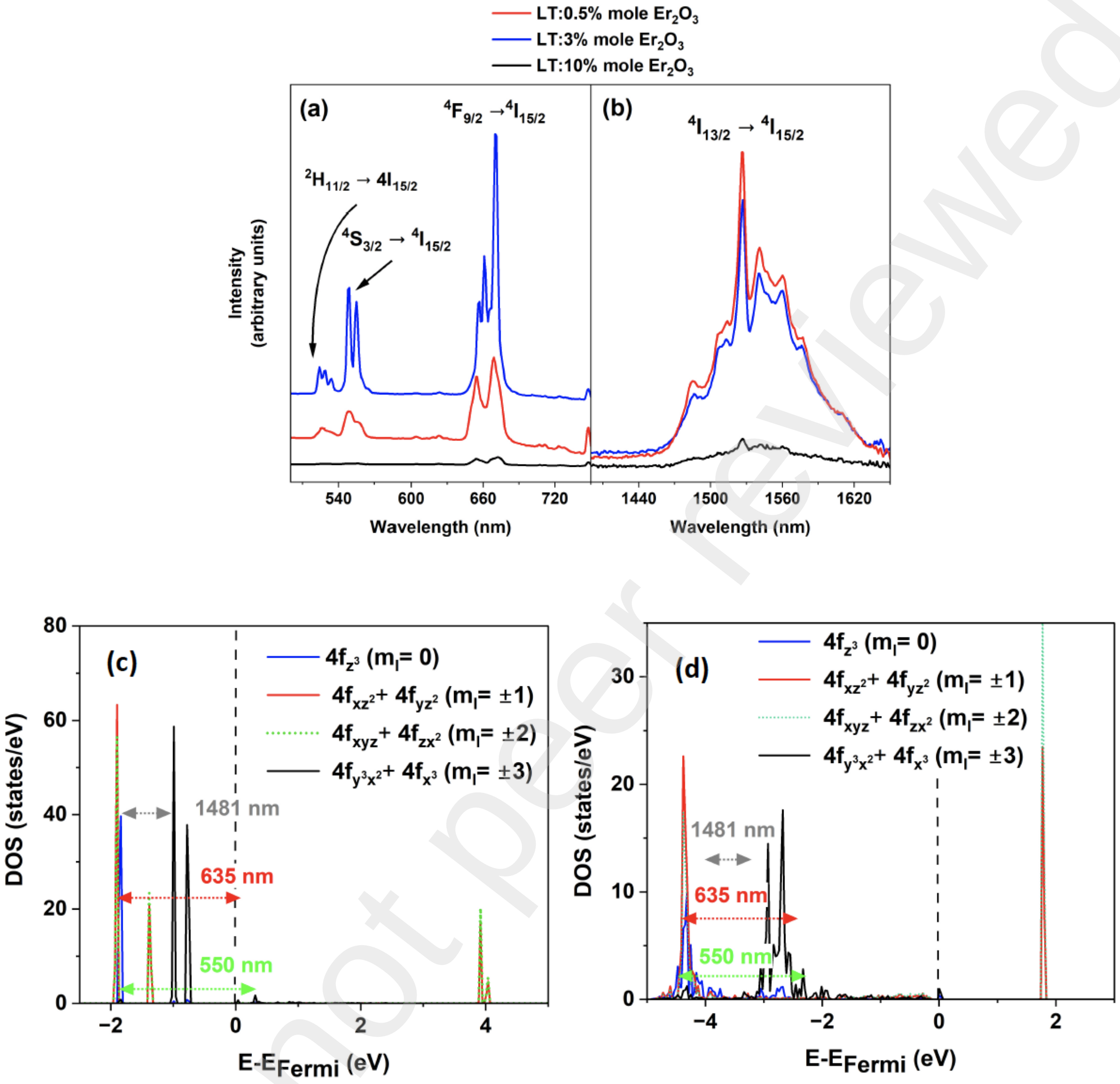

Fig. 7. (a) The fluorescence emission spectra for LT under 0.5, 3, and 10 mol% of Er_2O_3 with the Er transition assignments in the visible region and (b) the near IR. The Er transitions for the isolated Er^{+3} assignments are from Pokhrel et al. [69] (c) The DFT calculated Er-4f DOS using the HSE06 functional for LT:Er^{+3} with Er at the Li site and (d) at the Ta site. The double arrows show Er f–f transitions.

5. Conclusions

Nanoparticles of $LiTaO_3$-(0.5–10) mol. % Er_2O_3 were synthesized using the stepwise technique of first transforming commercially available tantalum oxide particles into nanoscale.

These particles were analyzed by XRD, DSC, and photoluminescence measurements. XRD showed no peak shifts between the host LT and its doped counterparts. However, DFT showed some changes in lattice parameters due to doping, which are not XRD detected. The DSC of the systems containing 3 mol. % Er_2O_3 shows lower reaction initiation temperature relative to LT, which could be attributed to the creation of additional reaction hotspots in the system. The activation energy for the $LiTaO_3$-3mol% Er_2O_3 was 263 kJ/mol which was higher than that for stoichiometric LT. The LT:Er^{+3} with 3 mol. % Er shows stronger visible photoluminescence emission compared to the system containing 0.5 % and 10 % Er. However, the system with 0.5 mol. % Er demonstrates improved near IR emission than both 3% and 10% Er doped LT.

We calculated electronic and optical properties on LT and LT:Er^{+3} under GGA settings by using DFT. These calculations showed that the location of the Er-4f bands depends on the metal site that Er occupies in the LT:Er^{+3}. The optical properties calculations show peaks in the bandgap region of the LT:Er^{+3}, which are absent in the host spectrum. These peaks verify the presence of intraband transitions. Bader-calculated charges showed that the Er and Ta oxidations are less than what are excepted from the chemical formula, which are attributed to the strong Er-O and Ta-O covalent bonding. Therefore, the Er ground state in the doped configurations is not the same as the free Er^{+3} (i.e., $^4I_{15/2}$). The electronic structure is also calculated using the hybrid functional HSE06 which accurately shows the location in energy of the individual 4f orbitals, thus allowing interband transition assignments. These assignments agree with the emissions from the photoluminescence measurements.

Acknowledgement. The author(s) would like to acknowledge funding provided by the National Science Foundation CREST Center for Multidisciplinary Research Excellence in Cyber-Physical Infrastructure Systems (NSF Award No. 2112650). The opinions expressed in this paper (or thesis or report or dissertation) are solely those of the author(s), and do not necessarily represent those of the NSF. The authors also acknowledge the Texas Advanced Computing Center (TACC) at The University of Texas at Austin for providing HPC resources that have contributed to the research results reported within this paper. URL: http://www.tacc.utexas.edu.

CRediT Author Statement

Mkhitar A. Hobosyan: Conceptualization, Methodology, Data curation, Supervision, Validation, Resources, Writing, reviewing, and editing; **Andrea Pelayo Carvajal:** Data curation, Validation, Resources; **Bhupendra Srivastava**: Data curation, Validation, Resources; **Tamanna Zakia:** Data curation, Validation, Resources; **Mohammed Jassim Uddin**: Data curation, Validation, Resources; **Karen S. Martirosyan**: Data curation, Validation, Resources; **Eric Rodriguez**: Data curation, Validation, Resources; **Kofi Nketia Ackaah-Gyasi**: Data curation, Validation, Resources **Nicholas Dimakis**: Conceptualization, Methodology, Calculations, Supervision, Validation, Resources, Writing, reviewing, and editing.

Data Availability

The raw and processed data that support the findings of this study are available from the corresponding author upon reasonable request.

Electronic Supplementary Materials

Computational and experimental study on undoped and Er-doped lithium tantalate nanofluorescent probes

Mkhitar A. Hobosyan[1], Andrea Pelayo Carvajal[1], Bhupendra B. Srivastava[2], Tamanna Zakia[2], Mohammed Jasim Uddin[2], Karen S. Martirosyan[1], Eric Rodriguez[3], Kofi Nketia Ackaah-Gyasi[4], and Nicholas Dimakis[2*]

[1]*Department of Physics and Astronomy, UTRGV, Edinburg, TX, 78539*

[2] *Photonics and Energy Research Laboratory-PERL, Department of Chemistry, UTRGV, Edinburg, TX, 78539*

[3]*Department of Mechanical Engineering, University of Texas Rio Grande Valley, Edinburg, 78539, USA*

[4]*Department of Computer Science, University of Texas Rio Grande Valley, Edinburg, 78539, USA*

---

[*] Author to whom correspondence should be made. E-mail: Nicholas.dimakis@utrgv.edu

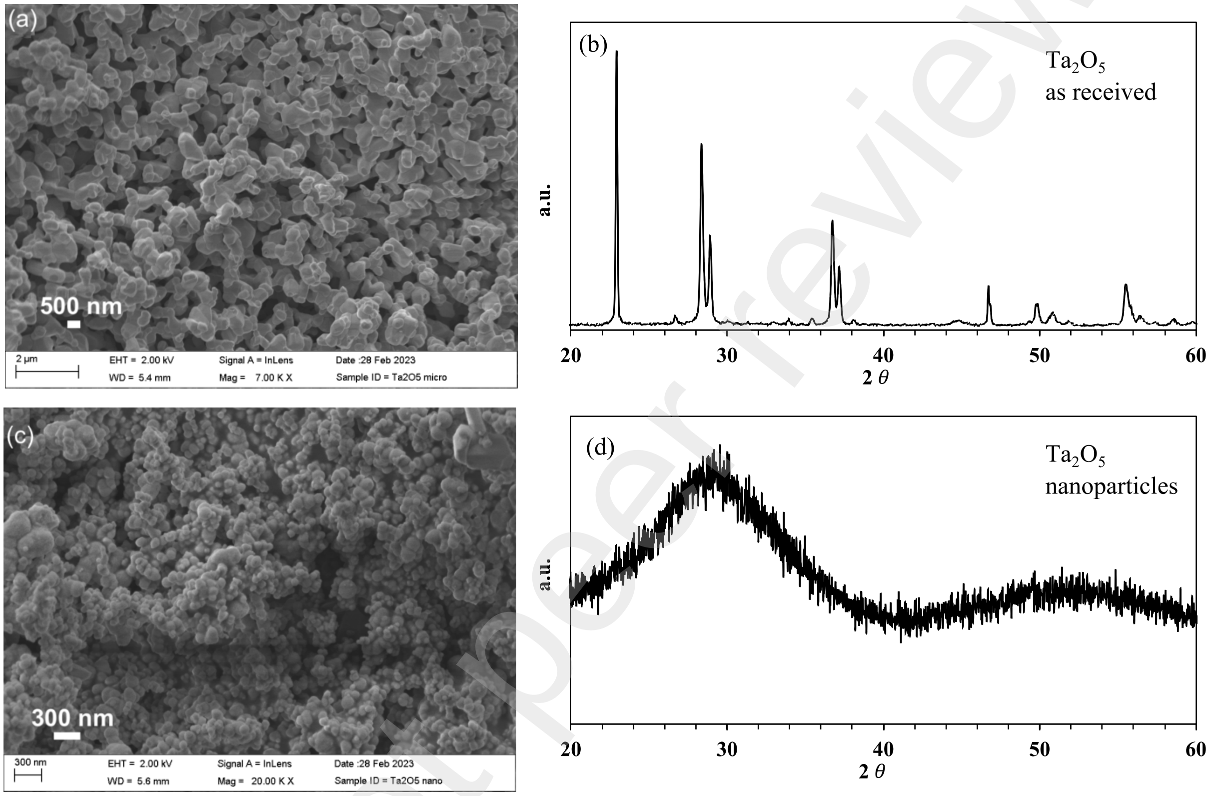

Fig. S1. SEM image of commercial Ta_2O_5 (a) with corresponding XRD (b) shows highly crystalline, micrometer-size particles, which were transformed to nano-meter size domain as evidenced by (c) SEM and (d) XRD analysis results.

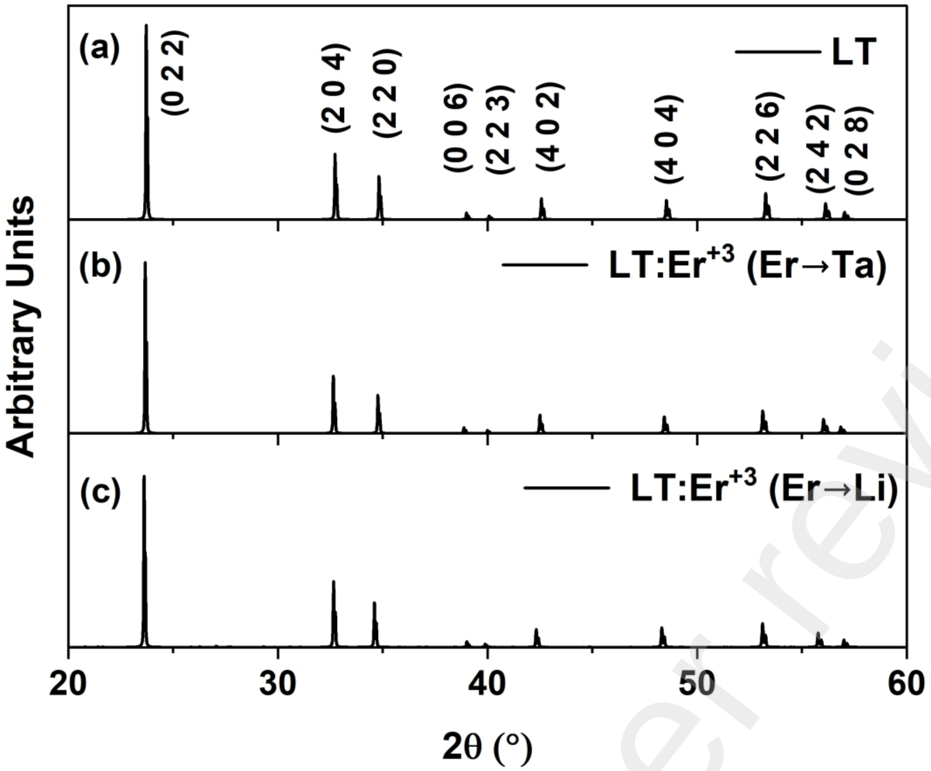

Fig. S2. Simulated XRD spectra with the corresponding Miller indices as calculated by VESTA using the supercell structure of Fig. 1. (a) LT and LT:Er^{+3} at 4.167% doping, where in (b) Er substitutes Ta and (c) Li.

References

[1] L. Xing, Y. Xu, R. Wang, W. Xu, Influence of temperature on upconversion multicolor luminescence in $Ho^{3+}/Yb^{3+}/Tm^{3+}$-doped LiNbO3 single crystal, Optics Letters, 38 (2013) 2535-2537.

[2] V.Y. Shur, A.R. Akhmatkhanov, D.S. Chezganov, A.I. Lobov, I.S. Baturin, M.M. Smirnov, Shape of isolated domains in lithium tantalate single crystals at elevated temperatures, Applied Physics Letters, 103 (2013) 242903.

[3] F. Juvalta, M. Jazbinsek, P. Günter, K. Kitamura, Electro-optical properties of near-stoichiometric and congruent lithium tantalate at ultraviolet wavelengths, J. Opt. Soc. Am. B, 23 (2006) 276-281.

[4] X. Yang, Y. Zhu, D. Ma, S. Long, Z. Liu, B. Wang, Luminescent properties of stoichiometric Er:LiTaO3 submicron particles synthesized by a modified solid-state combustion route, Ceramics International, 45 (2019) 10733-10739.

[5] Irzaman, Y. Pebriyanto, E.R. Apipah, I. Noor, A. Alkadri, Characterization of Optical and Structural of Lanthanum Doped LiTaO3 Thin Films, Integr Ferroelectr, 167 (2015) 137-145.

[6] G. Qiu, H. Ye, X. Wang, H. Fang, Y. Li, X. Yao, Intense piezoluminescence in $LiTaO_3$ phosphors doped with Pr^{3+} ions, Ceramics International, 45 (2019) 8553-8560.

[7] X. Li, R. Hu, X. Wang, Y. Li, X. Yao, Intense mechanoluminescence and photostimulated luminescence with less afterglow in Pr3+/Gd3+ co-doped LiTaO3 phosphors, Journal of Luminescence, 238 (2021) 118222.

[8] B. Sun, J. Wang, J. Gou, X. Liu, Y. Jiang, Influence of thermal annealing on structural and optical properties of RF-sputtered LiTaO3 thin films, Mater. Res. Express, 6 (2019) 026405-026408.

[9] N. Djohan, B. Harsono, J. Liman, H. Hardhienata, I. Husein, The effect of indium oxide (In2O3) dopant on the electrical properties of LiTaO3 thin film-based sensor, Ferroelectrics, 568 (2020) 55-61.

[10] N. Djohan, R. Estrada, D. Sari, M. Dahrul, A. Kurniawan, J. Iskandar, H. Hardhienata, Irzaman, The effect of annealing temperature variation on the optical properties test of LiTaO3 thin films based on Tauc Plot method for satellite technology, Iop C Ser Earth Env, 54 (2017).

[11] J.R. Luo, W.B. Luo, K.S. Zhang, X.W. Sun, Y. Shuai, T. Wang, C.G. Wu, W.L. Zhang, High specific detectivity infrared detector using crystal ion slicing transferred LiTaO3 single-crystal thin films, Sensor Actuat a-Phys, 300 (2019).

[12] H. Chen, Q. Gao, B. Qian, L. Zhao, Unusual Response of Thin LiTaO(3) Films to Intense Microwave Pulses, Materials (Basel), 12 (2019).

[13] G.J. Qiu, H.H. Ye, X.S. Wang, H. Fang, Y.X. Li, X. Yao, Intense piezoluminescence in LiTaO3 phosphors doped with Pr3+ ions, Ceram Int, 45 (2019) 8553-8560.

[14] X. Li, R. Hu, X.S. Wang, Y.X. Li, X. Yao, Intense mechanoluminescence and photostimulated luminescence with less afterglow in Pr3+/Gd3+ co-doped LiTaO3 phosphors, J Lumin, 238 (2021).

[15] X. Yang, Y.Z. Zhu, D.C. Ma, S.W. Long, Z.H. Liu, B. Wang, Luminescent properties of stoichiometric Er:LiTaO3 submicron particles synthesized by a modified solid-state combustion route, Ceram Int, 45 (2019) 10733-10739.

[16] X. Yang, S.P. Lin, D.C. Ma, S.W. Long, Y.Z. Zhu, H.S. Li, B.A. Wang, Up-conversion luminescence of LiTaO3:Er3+ phosphors for optical thermometry, Ceram Int, 46 (2020) 1178-1182.

[17] T. Yang, Y.G. Liu, L. Zhang, M.L. Hu, Q. Yang, Z.H. Huang, M.H. Fang, Powder synthesis and properties of LiTaO3 ceramics, Adv Powder Technol, 25 (2014) 933-936.

[18] V.A. Khokhlov, N.A. V'yugin, V.N. Dokutovich, I.D. Zakir'yanova, B.D. Antonov, Modification of the Cationic Composition of LiNbO3 and LiTaO3 Nanopowders in Calcium-Containing Chloride Melts, Russ Metall+, 2020 (2020) 144-149.
[19] H. Muthurajan, H.H. Kumar, N. Natarajan, V. Ravi, A novel technique to prepare LiTaO3 at low temperature, Ceramics International, 34 (2008) 669-670.
[20] Y.G. Liu, J.H. Hu, Z.H. Huang, M.H. Fang, Preparation of LiTaO3 nanoparticles by a sol-gel route, J Sol-Gel Sci Techn, 58 (2011) 664-668.
[21] P.P. Phule, T.A. Deis, D.G. Dindiger, Low-Temperature Synthesis of Ultrafine Litao3 Powders, J Mater Res, 6 (1991) 1567-1573.
[22] J. Szanics, M. Kakihana, A novel tantalic acid-based polymerizable complex route to LiTaO3 using neither alkoxides nor chlorides of tantalum, Chem Mater, 11 (1999) 2760-2763.
[23] J. Szanics, T. Okubo, M. Kakihana, Preparation of LiTaO3 powders at reduced temperatures by a polymerized complex method, J Alloy Compd, 281 (1998) 206-210.
[24] W. Kohn, L.J. Sham, Self-Consistent Equations Including Exchange and Correlation Effects, Phys. Rev., 140 (1965) A1133-A1138.
[25] P. Hohenberg, W. Kohn, Inhomogeneous Electron Gas, Phys. Rev., 136 (1964) B864-B871.
[26] F. Toksoy, S. Cabuk, DFT - based study of electronic structures and mechanical properties of LiTaO3: ferroelectric and paraelectric phases, Philosophical Magazine, 97 (2017) 2469-2483.
[27] H. Wang, F. Wu, H. Jiang, Electronic Band Structures of ATaO3(A = Li, Na, and K) from First-Principles Many-Body Perturbation Theory, The Journal of Physical Chemistry C, 115 (2011) 16180-16186.
[28] A. Riefer, S. Sanna, W.G. Schmidt, Lithium niobate-tantalate mixed crystals electronic and optical properties calculated from first principles, in: Proceedings of ISAF-ECAPD-PFM 2012, 2012, pp. 1-3.
[29] S. Huband, D.S. Keeble, N. Zhang, A.M. Glazer, A. Bartasyte, P.A. Thomas, Relationship between the structure and optical properties of lithium tantalate at the zero-birefringence point, J. Appl. Phys., 121 (2017) 024102.
[30] S. Sanna, S. Neufeld, M. Rüsing, G. Berth, A. Zrenner, W.G. Schmidt, Raman scattering efficiency in $LiTaO_3$ and $LiNbO_3$ crystals, Phys. Rev. B, 91 (2015) 224302.
[31] Ç. Süleyman, M. Amirullah, Urbach rule and optical properties of the LiNbO3 and LiTaO3, Journal of Optics A: Pure and Applied Optics, 1 (1999) 424.
[32] M. Wiegel, M.H.J. Emond, E.R. Stobbe, G. Blasse, Luminescence of alkali tantalates and niobates, Journal of Physics and Chemistry of Solids, 55 (1994) 773-778.
[33] H. Kato, A. Kudo, Water Splitting into H2 and O2 on Alkali Tantalate Photocatalysts ATaO3 (A = Li, Na, and K), The Journal of Physical Chemistry B, 105 (2001) 4285-4292.
[34] E.-J. Guo, J. Xing, H.-B. Lu, K.-J. Jin, J. Wen, G.-Z. Yang, Ultraviolet fast-response photoelectric effects in LiTaO3 single crystal, Journal of Physics D: Applied Physics, 43 (2010) 015402.
[35] K. Teramura, S.-i. Okuoka, H. Tsuneoka, T. Shishido, T. Tanaka, Photocatalytic reduction of CO2 using H2 as reductant over ATaO3 photocatalysts (A=Li, Na, K), Applied Catalysis B: Environmental, 96 (2010) 565-568.
[36] S. Tian, P. Feng, S. Ding, Y. Wang, Y. Wang, A color-tunable persistent luminescence material LiTaO3:Pr3+ for dynamic anti-counterfeiting, Journal of Alloys and Compounds, 899 (2022) 163325.
[37] L. Shi, Q. Shen, Z. Qiu, Concentration-dependent upconversion emission in Er-doped and Er/Yb-codoped LiTaO3 polycrystals, Journal of Luminescence, 148 (2014) 94-97.
[38] X. Yang, S. Lin, D. Ma, S. Long, Y. Zhu, H. Li, B. Wang, Up-conversion luminescence of LiTaO3:Er3+ phosphors for optical thermometry, Ceramics International, 46 (2020) 1178-1182.

[39] L. Shi, C. Li, Q. Shen, Z. Qiu, White upconversion emission in Er3+/Yb3+/Tm3+ codoped LiTaO3 polycrystals, Journal of Alloys and Compounds, 591 (2014) 105-109.
[40] J.P. Perdew, K. Burke, M. Ernzerhof, Generalized gradient approximation made simple, Phys. Rev. Lett., 77 (1996) 3865.
[41] J. Heyd, J.E. Peralta, G.E. Scuseria, R.L. Martin, Energy band gaps and lattice parameters evaluated with the Heyd-Scuseria-Ernzerhof screened hybrid functional, J. Chem. Phys., 123 (2005).
[42] G. Kresse, J. Hafner, Ab initio molecular dynamics for liquid metals, Phys. Rev. B, 47 (1993) 558(R)-561(R).
[43] G. Kresse, J. Hafner, Ab initio molecular-dynamics simulation of the liquid-metal–amorphous-semiconductor transition in germanium, Phys. Rev. B, 49 (1994) 14251-14269.
[44] G. Kresse, J. Furthmüller, Efficiency of ab-initio total energy calculations for metals and semiconductors using a plane-wave basis set, Comput. Mater. Sci., 6 (1996) 15-50.
[45] G. Kresse, J. Furthmüller, Efficient iterative schemes for ab initio total-energy calculations using a plane-wave basis set, Phys. Rev. B, 54 (1996) 11169-11186.
[46] G. Kresse, D. Joubert, From ultrasoft pseudopotentials to the projector augmented-wave method, Phys. Rev. B, 59 (1999) 1758-1775.
[47] P.E. Blöchl, Projector augmented-wave method, Phys. Rev. B, 50 (1994) 17953-17979.
[48] A.V. Krukau, O.A. Vydrov, A.F. Izmaylov, G.E. Scuseria, Influence of the exchange screening parameter on the performance of screened hybrid functionals, J. Chem. Phys., 125 (2006) 224106-224105.
[49] W. Kohn, L.J. Sham, Self-consistent equations including exchange and correlation effects, Physical review, 140 (1965) A1133.
[50] A.J. Garza, G.E. Scuseria, Predicting band gaps with hybrid density functionals, The journal of physical chemistry letters, 7 (2016) 4165-4170.
[51] P. Hohenberg, W. Kohn, Inhomogeneous electron gas, Phys. Rev., 136 (1964) B864.
[52] J. Heyd, G.E. Scuseria, M. Ernzerhof, Hybrid functionals based on a screened Coulomb potential, The Journal of chemical physics, 118 (2003) 8207-8215.
[53] S. Grimme, J. Antony, S. Ehrlich, H. Krieg, A consistent and accurate ab initio parametrization of density functional dispersion correction (DFT-D) for the 94 elements H-Pu, J. Chem. Phys., 132 (2010) 154104-154119.
[54] R. Bader, Atoms in Molecules: A Quantum Theory: Oxford Univ. Press, in, Oxford, 1990.
[55] W. Tang, E. Sanville, G. Henkelman, A grid-based Bader analysis algorithm without lattice bias, J. Phys. Condens. Matter, 21 (2009) 084204.
[56] E. Sanville, S.D. Kenny, R. Smith, G. Henkelman, Improved grid-based algorithm for Bader charge allocation, J. Comput. Chem., 28 (2007) 899-908.
[57] G. Henkelman, A. Arnaldsson, H. Jónsson, A fast and robust algorithm for Bader decomposition of charge density, Comput. Mater. Sci., 36 (2006) 354-360.
[58] M. Yu, D.R. Trinkle, Accurate and efficient algorithm for Bader charge integration, J. Chem. Phys., 134 (2011) 064111.
[59] A. Delin, P. Ravindran, O. Eriksson, J.M. Wills, Full-potential optical calculations of lead chalcogenides, Int. J. Quantum Chem., 69 (1998) 349-358.
[60] P. Rivera, W. Yao, X. Xu, Optical Properties of TMD Heterostructures, in: P. Avouris, T. Low, T.F. Heinz (Eds.) 2D Materials: Properties and Devices, Cambridge University Press, Cambridge, 2017, pp. 310-328.
[61] S.L. Adler, Quantum Theory of the Dielectric Constant in Real Solids, Phys. Rev., 126 (1962) 413-420.
[62] M.J. Starink, The determination of activation energy from linear heating rate experiments: a comparison of the accuracy of isoconversion methods, Thermochimica Acta, 404 (2003) 163-176.

[63] M.A. Hobosyan, K.G. Kirakosyan, S.L. Kharatyan, K.S. Martirosyan, PTFE–Al2O3 reactive interaction at high heating rates, Journal of Thermal Analysis and Calorimetry, 119 (2015) 245-251.
[64] S.C. Navale, A.B. Gaikwad, V. Ravi, A coprecipitation technique to prepare LiTaO3 powders, Materials Letters, 60 (2006) 1047-1048.
[65] T. Wang, X. Tan, Y. Wei, H. Jin, Accurate bandgap predictions of solids assisted by machine learning, Materials Today Communications, 29 (2021) 102932.
[66] M. Hatanaka, S. Yabushita, Theoretical Study on the f−f Transition Intensities of Lanthanide Trihalide Systems, The Journal of Physical Chemistry A, 113 (2009) 12615-12625.
[67] S. Cabuk, The nonlinear optical susceptibility and electro-optic tensor of ferroelectrics: first-principle study, Central European Journal of Physics, 10 (2012) 239-252.
[68] P.K. Joshi, K. Kumar, D. Mali, G. Arora, L. Meena, B.L. Ahuja, Validation of hybrid WC1LYP functional for ferroelectric LiNbO3 and LiTaO3 using Compton spectroscopy and first-principles computations, Materials Today Communications, 31 (2022) 103288.
[69] M. Pokhrel, G.A. Kumar, C.G. Ma, M.G. Brik, B.W. Langloss, I.N. Stanton, M.J. Therien, D.K. Sardar, Y. Mao, Electronic and optical properties of Er-doped Y2O2S phosphors, Journal of Materials Chemistry C, 3 (2015) 11486-11496.